JOURNAL OF SYNCHROTRON RADIATION

ISSN 1600-5775

Upgrade of laser pump time-resolved X-ray probes in Beijing synchrotron

Can Yu,[a,b] Yan Zhang,[a] Ge Lei,[c] Hao Wang,[a,b] Yu-hang Wang,[a,b] Bing-Bing Zhang,[a] Da-Rui Sun,[a] Jia-Li Zhao,[a] Yang-Fan Zhou,[a] Qiu-Ju Li,[a] Zhen-hua Gao,[a] Fei Zhan[a,d] and Ye Tao[a]*

[a]Beijing Synchrotron Radiation Facility, Institute of High Energy Physics, Chinese Academy of Sciences, 19B Yuquan Road, Beijing 100049, People's Republic of China, [b]University of Chinese Academy of Sciences, 19B Yuquan Road, Beijing 100049, People's Republic of China, [c]Accelerator Division, Institute of High Energy Physics, Chinese Academy of Sciences, 19B Yuquan Road, Beijing 100049, People's Republic of China, and [d]Chemistry and Chemical Engineering Guangdong Laboratory, Shantou, Guangdong 515031, People's Republic of China.
*Correspondence e-mail: taoy@ihep.ac.cn

Received 12 August 2019
Accepted 12 September 2019

Edited by M. Yabashi, RIKEN SPring-8 Center, Japan

Keywords: laser pump/X-ray probe; time-resolved X-ray absorption spectroscopy; time-resolved X-ray diffraction; thin films.

The upgrade of the laser pump time-resolved X-ray probes, namely time-resolved X-ray absorption spectroscopy (TR-XAS) and X-ray diffraction (TR-XRD), implemented at the Beijing Synchrotron Radiation Facility, is described. The improvements include a superbunch fill, a high-efficiency fluorescence collection, an efficient spatial overlap protocol and a new data-acquisition scheme. After upgrade, the adequate TR-XAS signal is now obtained in a 0.3 mM solution, compared with a 6 mM solution in our previous report. Furthermore, to extend application in photophysics, the TR-XAS probe is applied on $SrCoO_{2.5}$ thin film. And for the first time, TR-XAS is combined with TR-XRD to simultaneously detect the kinetic trace of structural changes in thin film.

1. Introduction

The pump–probe time-resolved X-ray technique is a powerful tool for studying transient structure in non-equilibrium processes. In a typical pump–probe experiment, short laser pulses excite a sample to its non-equilibrium states, which are probed by X-ray pulses at different time delays after laser excitation. Versatile X-ray probes can be applied in pump–probe measurements. Here we only discuss time-resolved X-ray absorption spectroscopy (TR-XAS) and time-resolved X-ray diffraction (TR-XRD) using monochromatic X-rays in synchrotrons. Mostly applied in photochemistry and photocatalysis studies, TR-XAS could provide transient electronic and geometric structure information (Chen, 2005; Chen *et al.*, 2010, 2014; Bressler & Chergui, 2010; Chen & Zhang, 2013; Smolentsev & Sundström, 2015). Since the development of high-repetition-rate TR-XAS (Lima *et al.*, 2011; March *et al.*, 2011) the signal-to-noise ratio (SNR) has been drastically improved. TR-XAS was also applied in photophysics, especially in thin films (Wen *et al.*, 2015). TR-XRD has been widely used in thin-film systems (Daranciang *et al.*, 2012; Schick *et al.*, 2014; Wen *et al.*, 2013). Another trend of time-resolved experiments is the combination of different methods, such as the simultaneous measurement of X-ray emission spectroscopy (XES) and X-ray wide-angle scattering (Haldrup *et al.*, 2012), and XES and X-ray protein crystallography in X-ray free-electron lasers (XFELs) (Kern *et al.*, 2013). Simultaneous observation of transient processes using different probes helps to obtain a more complete picture of structure dynamics.

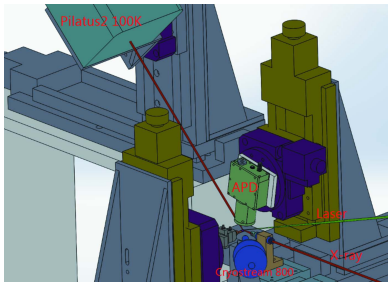

We have developed TR-XRD in thin films (Sun *et al.*, 2016) and TR-XAS in photochemistry at the Beijing Synchrotron Radiation Facility (BSRF) (Wang *et al.*, 2017). Although time-resolved X-ray absorption near-edge fine-structure spectroscopy (TR-XANES) from a 6 m*M* iron complex solution has been demonstrated (Wang *et al.*, 2017), there is considerable discrepancy between this demonstration and practical applications. Most practical photochemical systems feature in low concentration below 1 m*M*, calling for remarkable improvement of SNR for our TR-XAS detection. Moreover, TR-XAS is needed to extend to thin-film samples and we further proposed the integration of the TR-XRD and TR-XAS setups to achieve a simultaneous detection. To address these requirements, we upgraded the laser pump/X-ray probe instrumentation, with details given in Section 2. In Section 3, two experimental demonstrations are briefly presented.

2. Experiment upgrades

2.1. Super bunch and X-ray source

As a parasitic light source of the Beijing Electron–Positron Collider, BSRF runs in two modes, the high-energy physics mode with beam current in decay mode and the dedicated synchrotron mode with top-up injection. Hybrid injection has been successfully achieved in both modes, optimizing for time-resolved experiments by use of a single bunch (camshaft bunch) current of 2.5 mA (Wang *et al.*, 2017). The increase of the camshaft bunch current is the most straightforward way to increase the X-ray photons used for pump–probe measurements. As shown in Fig. 1, a superbunch with a 9 mA beam current is successfully realized in top-up mode.

Two kinds of polycapillaries were applied for secondary X-ray focusing. One can focus X-rays to ∼80 µm with a working distance of 21 mm, while the other can focus down to ∼30 µm with only 5 mm working distance. The smaller X-ray spot size is needed for excitation by an optical parametric amplifier (OPA), newly installed, which has low laser pulse energy (1–9 µJ per pulse) to ensure sufficient excitation.

2.2. Enhancement of X-ray fluorescence collection efficiency

Even with the help of the super bunch, the X-ray photon flux is still only $\sim 10^3$ photons pulse^{-1}, two to three orders of magnitude weaker than the undulator sources at third-generation synchrotrons. Therefore, the fluorescence collection enhancement of the TR-XAS is essential to compensate for the lower flux. The direct way is to minimize the sample–detector distance to maximize collection efficiency. However, this is a trade-off between soller slit unit, detector case shape, liquid jet chamber and avoidance of sample splash on detector. Fig. 2 presents the optimization result of the new setup. The soller slit unit is fixed on the nose of an avalanche photodiode (APD) case and consists of a $Z - 1$ fluorescence filter, a 3D printing minor soller slit and a light-tight Be window. As the soller slit gets closer to the liquid jet, the area of incidence in front of the slit decreases. The slit-blade thickness should be minimized to obtain a high transmission efficiency. With a reduced blade thickness of 0.13 mm, 78.6% transmission efficiency is realized under the new design. The incident angle of laser towards the liquid jet is redesigned to be as small as 16° to avoid the damage of capillary and soller slit by laser. Homemade APD and soller slit units fit well with the optimization requirements, including finer detector cross-section, unsymmetrical shape and customized electronics circuit, as shown in Fig. 2. Also, the soller slit is designed with an unsymmetrical profile to avoid laser interaction. The distance between sample centre and sensor face is pushed down to only 6 mm after optimization, representing a fluorescence collection solid angle of 1.28 sterad for each APD (10 mm × 10 mm sensor area). About 20.4% of the total fluorescence, without considering the absorption of the filter and the Be window, can be received using two APDs, three times higher efficiency than the previous setup. Under this compact design, the laser-illuminated aqueous samples have been proven not to splash on the filter.

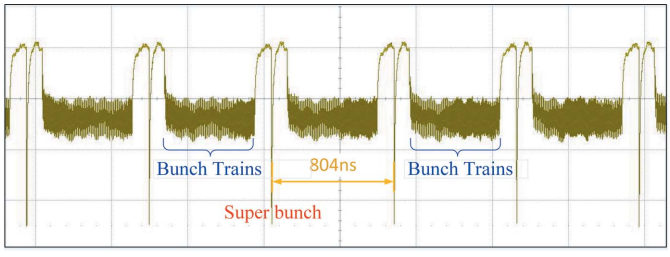

Figure 1
Super bunches in the hybrid fill pattern of the BSRF, where a camshaft bunch is placed in the middle of a large gap between bunch trains. The beam current of super bunch and small bunches within bunch trains is 9 mA and 2.5 mA, respectively. The total beam current is 250 mA. The data are acquired by a 4 GHz oscilloscope using a fast-response photodiode.

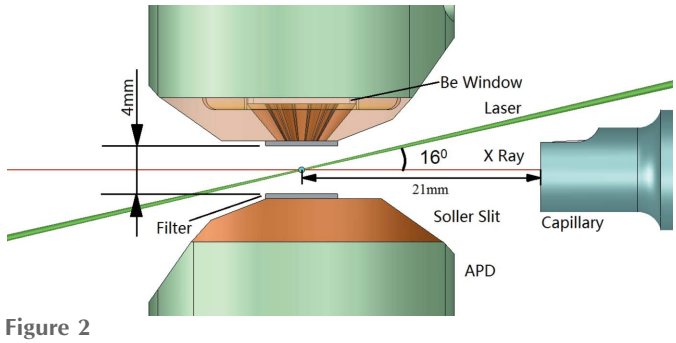

Figure 2
Top view of the sample environment assembly for high-efficiency X-ray fluorescence collection design. The APD and soller slit were optimized in an unsymmetrical design for maximum collection. The liquid jet is represented by a blue spot. The working distance of the polycapillary is 21 mm.

2.3. New protocol of laser and X-ray spatial overlap

The long-term spatial and temporal overlap stability is a prerequisite to the success of TR-XAS experiments. The previous spatial overlap is realized by the manual adjustment of the laser and X-ray spot centre on a YAG fluorescence screen (Wang *et al.*, 2017). Only coarse overlap can be reached according to this scheme and further optimization of the

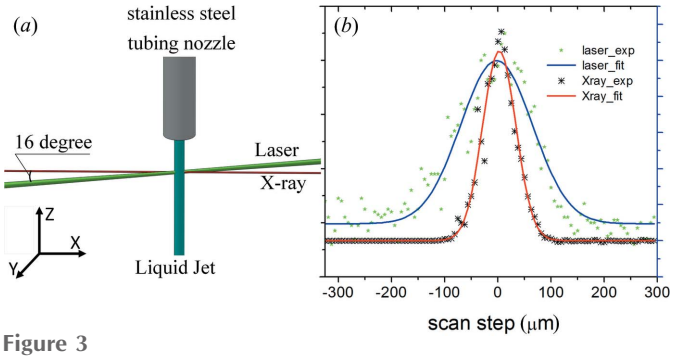

Figure 3
(*a*) Laser (green) and X-ray beam (red) overlap in the centre of the liquid jet. (*b*) Spatial overlap scanning of laser and X-ray by stainless steel tubing. The position and size of the spot can be obtained from the Gaussian fitting of the scan.

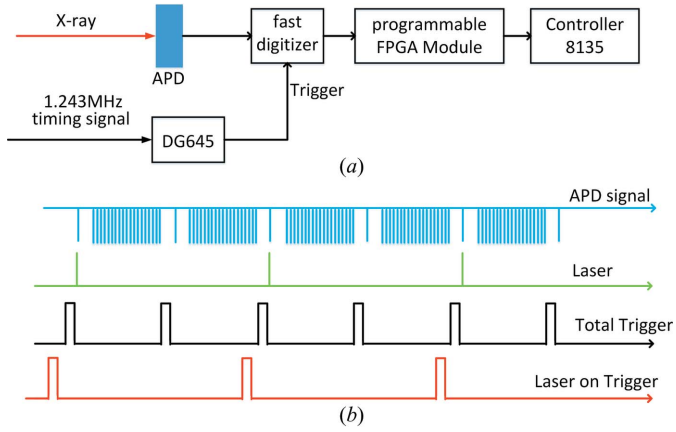

Figure 4
(*a*) FPGA scheme for transient data collection and on-line processing based on a commercialized FPGA system (NI). (*b*) Trigger scheme for both extracting the signal of the super bunch at 1.243 MHz and distinguishing the laser-on and laser-off signal at 621.5 kHz.

transient signal is necessary to obtain precise overlap. However, this process is difficult to work on the unknown sample system, since it is hard to know if the transient signal exists in advance. Generally, we had to use a reference sample to reach precise overlap and replaced it with the pending sample. The tubing had to be rinsed to avoid contamination. The sample switch process is time-consuming and the set precise overlap is prone to degrade, calling for a more efficient and reliable scheme to realize precise spatial overlap.

In a typical photochemical experiment, a solution sample is delivered to a stainless steel tubing nozzle to form a cylindrical liquid jet driven by a peristaltic pump, as shown in Fig. 3(*a*). The laser and X-ray focal spots must overlap in the centre of the sample jet. We proposed a knife scanning scheme using the stainless tubing nozzle as the scan knife edge. The nozzle drops 2 mm to scan the laser and X-ray beam simultaneously, in both *Y* and *Z* directions. Therefore, we could acquire the central position and spot size of both the laser and the X-ray at the same time. By means of this new scheme, the spatial overlap of the liquid jet centre, laser and X-ray beam spot sizes can be achieved precisely and efficiently. No reference sample is needed. The scanning result using a 500 μm-diameter nozzle along the *Y* direction is shown in Fig. 3(*b*). The X-ray spot size, laser spot size and overlap deviation are 80, 160 and 5 μm, respectively.

2.4. Improvement on TR-XAS data acquisition

TR-XAS data collection is generally carried out by obtaining the laser-on minus laser-off difference spectrum. This scheme helps to cancel the systematic error in the difference spectrum, as the on and off signals are acquired almost simultaneously. The previous data-acquisition scheme was based on Nuclear Instrument Module (NIM) hardware, where we used gated constant fraction discriminators (CFDs) to select out the signal over threshold by adjusting a potentiometer (Wang *et al.*, 2017). Because the on and off signals were processed by different channels of the CFD, the long-term drift of the threshold settings would introduce system noise. As the data collection will take quite a long time, the data quality would be greatly influenced using a NIM scheme, especially for low-concentration photocatalytic systems. Therefore, a new data-acquisition method based on the field programmable gate array (FPGA) scheme is developed, as shown in Fig. 4.

The acquisition system is controlled by a PXIe-8135 controller (NI). X-ray fluorescence signals collected by APDs are first converted to digital signals by digitizer (NI5772, NI) and then online processed by a FPGA module (PXIe-7976R, NI) to obtain the difference signal, defined as laser-on minus laser-off. A delay generator (DG645, SRS), triggered by the 1.243 MHz timing signal, provides frequency division and suitable delays to the FPGA system. As shown in Fig. 4(*b*), the Total Trigger (1.243 MHz) for both laser-on and laser-off signal is set before the super bunch, and the APD signal is sampled after trigger. The laser-on trigger (621.5 kHz) from division of the timing signal is used to distinguish between laser-on and laser-off signals.

2.5. Simultaneous measurement of transient XRD and XAS

During setup of TR-XAS for thin film, we proposed to measure both transient XRD and XAS simultaneously. Since the TR-XAS needs to scan the energy, the combination measurement here represents the simultaneous time-delay scan of Bragg peak shifts and the absorption difference at fixed energy. The energy selection is dependent on the difference features from the TR-XAS. The combination scheme provides a unique way to obtain the systematic kinetic traces in both the local structure and collective motions of the crystal unit cell, simultaneously. The setup is shown in Fig. 5, where a Pilatus detector is used to collect Bragg reflections of the film and an APD is placed above the sample to collect fluorescence of the interested element. To maximize the X-ray fluorescence collection efficiency, the head of the APD is placed parallel to the film, as close to the sample as possible without blocking the laser and X-ray beam. To balance the thermal effects caused by laser and collection efficiency, the laser repetition rate is compromised, generally set at less than 100 kHz. The sample was cooled to expedite heat dissipation

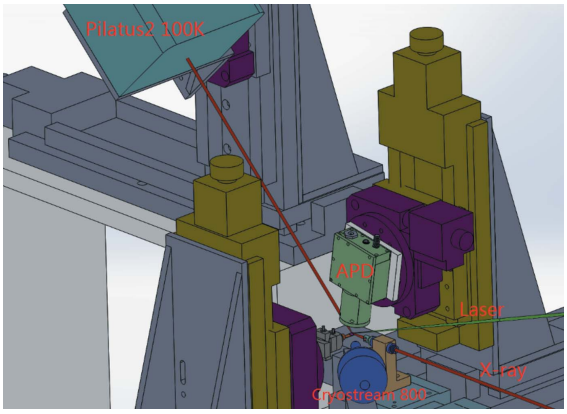

Figure 5
Setup of simultaneous measurement of transient XRD and XAS. Both X-ray (red line) and laser (green line) are incident from the right side. The APD (light green) is placed above the sample to collect fluorescence and the Pilatus is placed at the upper left to detect reflection peak. The sample is cooled by blowing 100 K nitrogen using a cryojet (blue line).

by purging with 100 K nitrogen gas using an Oxford Cryosystems cooler (Cryostream 800). The XAS fluorescence and diffraction peak were recorded simultaneously by APD and Pilatus, respectively, at different time delay to obtain the decay curve.

2.6. Extension of laser wavelength range

The high-repetition-rate and high-power laser system has been described (Wang *et al.*, 2017) with second-harmonic generation (SHG) and third-harmonic generation (THG) for excitation. However, the suitable excitation wavelength varies with the samples so the laser system is upgraded with an OPA and a fourth harmonic module is installed. The OPA provides continuous excitation wavelength from 210 to 11000 nm. The fourth harmonic module offers a maximum of 12 μJ pulse^{-1} at 257.5 nm. The pulse energy of the harmonics and the OPA are shown in Fig. 6. To provide a stable operation environment, the laser system with OPA is relocated in a separated laser hutch adjacent to the X-ray experiment hutch. The laser transport efficiency to the sample is up to 90%.

3. Applications of the upgrade

3.1. TR-XAS collection in sub-millimolar concentration solution

In our previous report, the TR-XANES was obtained from a 6 m*M* solution of a photo-induced crossover iron(II) complex, 1,10-phenanthroline iron sulfate (Wang *et al.*, 2017). After the upgrades described in Section 2 we obtained the transient XANES with concentration pushed down to 0.3 m*M* for the same sample, as shown in Fig. 7. As the sample concentration decreases, we could increase the repetition rate from the previous 155 kHz to the current 621.5 kHz. In the meantime, we also collected the time-resolved extended X-ray absorption fine-structure spectroscopy (TR-EXAFS) data in a 0.75 m*M* solution. The difference EXAFS data are presented

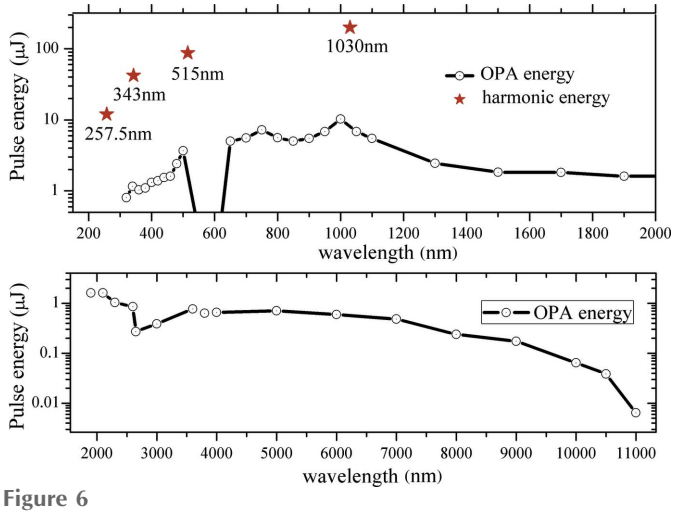

Figure 6
Pulse energy of harmonics and OPA. The harmonic energy is marked by stars.

and compared with the data collected at the Advanced Photon Source (APS) in Fig. 8. The red line is TR-EXAFS data of the same sample but in 5 m*M* and collected at the APS (Zhan *et al.*, 2017). Our data are coincident with the red line. Using the difference EXAFS analysis method that we developed (Zhan *et al.*, 2017), the first shell bond change could be obtained.

3.2. Simultaneous measurement of both TR-XRD and TR-XAS on an $SrCoO_{2.5}$ thin film

For a *c*-axis-oriented single-crystalline brownmillerite $SrCoO_{2.5}$ thin film (BM-SCO) on a $(LaAlO_3)_{0.3}(SrAlTaO_3)_{0.7}$ (LSAT) substrate, TR-XRD has captured a giant out-of-plane photo-induced strain, $\Delta c/c > 1\%$ (unpublished data). The BM-SCO has alternating octahedral CoO_6 and tetrahedral CoO_4 layers, so the local structure change around the Co atom is a new surge of interest upon laser excitation. The Co *K*-edge of TR-XAS of a 47 nm thin film was collected as shown in Fig. 9. The TR-XAS data are noisy because of the poor photon counts but we see four features in the difference spectrum

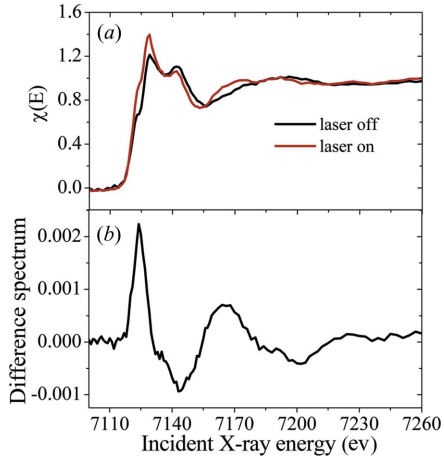

Figure 7
(*a*) Transient XANES of $[Fe^{II}(phen)_3]^{2+}$ at a concentration of 0.3 m*M*. (*b*) Difference spectrum from laser-on minus laser-off in (*a*).

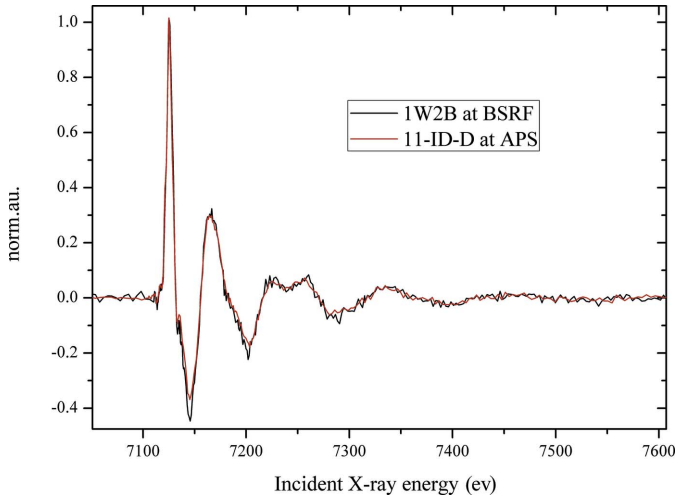

Figure 8
TR-EXAFS difference spectrum of $[Fe^{II}(phen)_3]^{2+}$. The concentration is 0.75 m*M* collected at 1W2B at the BSRF (black line), while the concentration is 5 m*M* collected at 11-ID-D at the APS (red). The two sets of data have been normalized for comparison.

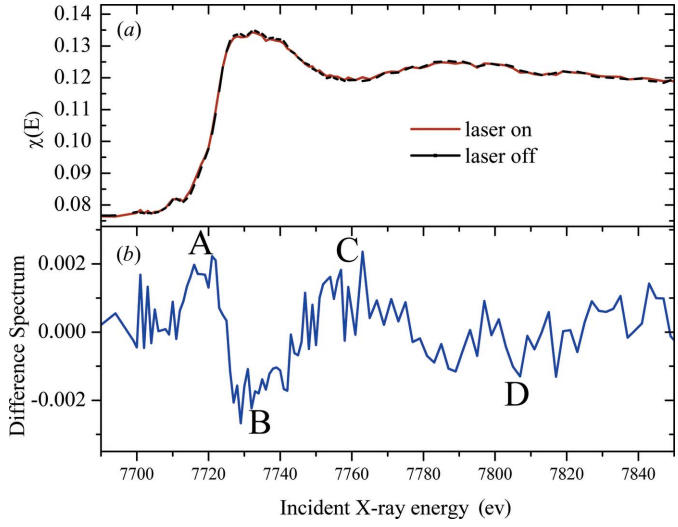

Figure 9
(*a*) Excited state (red solid) at 150 ps after photoexcitation, ground state (black dashed) at 26 µs after photoexcitation. The excitation wavelength is 515 nm with a fluence of 20 mJ cm^{-2}. (*b*) Difference spectrum from laser-on minus laser-off.

[Fig. 9(*b*)]. For simultaneous TR-XAS and TR-XRD measurements, a 20 nm BM-SCO film was chosen to ensure the full excitation of the film because of 30 nm laser penetration depth at 515 nm wavelength for BM-SCO. X-ray energy is fixed at 7718 eV, corresponding to feature A in Fig. 9(*b*). To reduce thermal effects, the laser repetition rate is set at 38 kHz. The 008 reflection of the thin film and the difference feature A were collected at different time delays. Fig. 10 gives the decay of feature A in TR-XAS, indicating a similar trend to the angular shift decay from TR-XRD. A detailed analysis of the experimental results will be presented elsewhere.

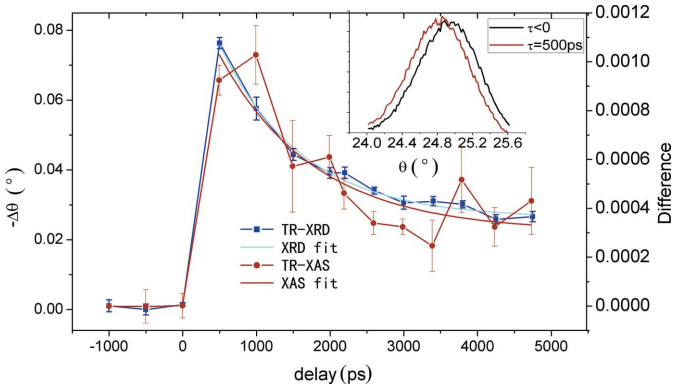

Figure 10
Simultaneous measurement of the decay of transient XRD and XAS of a 20 nm BM-SCO film. The evolution data could be fitted to a single exponential function. The lifetime of TR-XAS is 1.2 ns and the lifetime of TR-XRD is 1.1 ns. The incident laser fluence was 10 mJ cm^{-2}. A $Z-1$ Fe abs6 filter is used for TR-XAS detection. The inset shows the BM-SCO 008 reflection position before and after excitation.

4. Summary

Efforts have been made to improve the SNR of our TR-XAS instrumentation to meet the requirements of low-concentration detection in practical systems. The improvements include a super-bunch injection realized in top-up mode, a higher fluorescence collection unit design, a reliable and efficient spatial overlap protocol and a new data-acquisition system based on an FPGA scheme. With these improvements, adequate transient XAS signal in submillimolar concentration solution has been obtained.

TR-XAS was also applied in thin-film samples. Moreover, we proposed and realized the simultaneous measurement of TR-XAS and TR-XRD, and successfully applied it to the BM-SCO thin film. Next, the SNR of TR-XAS in film samples will be further improved.

Acknowledgements

We appreciate the help from Zhen-Jie Li at the APD detector and Guang-Lei Xu in timing. We also thank beamline scientists at the 1W2B beamline for their assistance.

Funding information

This research was supported by the High Energy Photon Source-Test Facility project and the National Natural Science Foundation of China (No. U1332205).

References

Bressler, C. & Chergui, M. (2010). *Annu. Rev. Phys. Chem.* **61**, 263–282.
Chen, L. X. (2005). *Annu. Rev. Phys. Chem.* **56**, 221–254.
Chen, L. X. & Zhang, X. Y. (2013). *J. Phys. Chem. Lett.* **4**, 4000–4013.
Chen, L. X., Zhang, X., Lockard, J. V., Stickrath, A. B., Attenkofer, K., Jennings, G. & Liu, D.-J. (2010). *Acta Cryst.* A**66**, 240–251.
Chen, L. X., Zhang, X. & Shelby, M. L. (2014). *Chem. Sci.* **5**, 4136–4152.
Daranciang, D., Highland, M. J., Wen, H. D., Young, S. M., Brandt, N. C., Hwang, H. Y., Vattilana, M., Nicoul, M., Quirin, F.,

Goodfellow, J., Qi, T. T., Grinberg, I., Fritz, D. M., Cammarata, M., Zhu, D. L., Lemke, H. T., Walko, D. A., Dufresne, E. M., Li, Y. L., Larsson, J., Reis, D. A., Sokolowski-Tinten, K., Nelson, K. A., Rappe, A. M., Fuoss, P. H., Stephenson, G. B. & Lindenberg, A. M. (2012). *Phys. Rev. Lett.* **108**, 087601.

Haldrup, K., Vankó, G., Gawelda, W., Galler, A., Doumy, G., March, A. M., Kanter, E. P., Bordage, A., Dohn, A., van Driel, T. B., Kjaer, K. S., Lemke, H. T., Canton, S. E., Uhlig, J., Sundström, V., Young, L., Southworth, S. H., Nielsen, M. M. & Bressler, C. (2012). *J. Phys. Chem. A*, **116**, 9878–9887.

Kern, J., Alonso-Mori, R., Tran, R., Hattne, J., Gildea, R. J., Echols, N., Glöckner, C., Hellmich, J., Laksmono, H., Sierra, R. G., Lassalle-Kaiser, B., Koroidov, S., Lampe, A., Han, G. Y., Gul, S., Difiore, D., Milathianaki, D., Fry, A. R., Miahnahri, A., Schafer, D. W., Messerschmidt, M., Seibert, M. M., Koglin, J. E., Sokaras, D., Weng, T. C., Sellberg, J., Latimer, M. J., Grosse-Kunstleve, R. W., Zwart, P. H., White, W. E., Glatzel, P., Adams, P. D., Bogan, M. J., Williams, G. J., Boutet, S., Messinger, J., Zouni, A., Sauter, N. K., Yachandra, V. K., Bergmann, U. & Yano, J. (2013). *Science*, **340**, 491–495.

Lima, F. A., Milne, C. J., Amarasinghe, D. C. V., Rittmann-Frank, M. H., van der Veen, R. M., Reinhard, M., Pham, V. T., Karlsson, S., Johnson, S. L., Grolimund, D., Borca, C., Huthwelker, T., Janousch, M., van Mourik, F., Abela, R. & Chergui, M. (2011). *Rev. Sci. Instrum.* **82**, 063111.

March, A. M., Stickrath, A., Doumy, G., Kanter, E. P., Krassig, B., Southworth, S. H., Attenkofer, K., Kurtz, C. A., Chen, L. X. & Young, L. (2011). *Rev. Sci. Instrum.* **82**, 073110.

Schick, D., Herzog, M., Wen, H., Chen, P., Adamo, C., Gaal, P., Schlom, D. G., Evans, P. G., Li, Y. & Bargheer, M. (2014). *Phys. Rev. Lett.* **112**, 097602.

Smolentsev, G. & Sundström, V. (2015). *Coord. Chem. Rev.* **304–305**, 117–132.

Sun, D.-R., Xu, G.-L., Zhang, B.-B., Du, X.-Y., Wang, H., Li, Q.-J., Zhou, Y.-F., Li, Z.-J., Zhang, Y., He, J., Yue, J.-H., Lei, G. & Tao, Y. (2016). *J. Synchrotron Rad.* **23**, 830–835.

Wang, H., Yu, C., Wei, X., Gao, Z., Xu, G.-L., Sun, D.-R., Li, Z., Zhou, Y., Li, Q.-J., Zhang, B.-B., Xu, J.-Q., Wang, L., Zhang, Y., Tan, Y.-L. & Tao, Y. (2017). *J. Synchrotron Rad.* **24**, 667–673.

Wen, H., Sassi, M., Luo, Z., Adamo, C., Schlom, D. G., Rosso, K. M. & Zhang, X. (2015). *Sci. Rep.* **5**, 15098.

Wen, H. D., Chen, P., Cosgriff, M. P., Walko, D. A., Lee, J. H., Adamo, C., Schaller, R. D., Ihlefeld, J. F., Dufresne, E. M., Schlom, D. G., Evans, P. G., Freeland, J. W. & Li, Y. L. (2013). *Phys. Rev. Lett.* **110**, 037601.

Zhan, F., Tao, Y. & Zhao, H. (2017). *J. Synchrotron Rad.* **24**, 818–824.